Journal of Power and Energy Engineering, 2025, 13(6), 76-94
https://www.scirp.org/journal/jpee
ISSN Online: 2327-5901
ISSN Print: 2327-588X

Synthesis of High Entropy Carbon Nanofibers and Study of Their Bifunctional Oxygen Performance

Zilong Li

College of Physics and Electronic Information Engineering, Guilin University of Technology, Guilin, China
Email: 18376606410@163.com

How to cite this paper: Li, Z.L. (2025) Synthesis of High Entropy Carbon Nanofibers and Study of Their Bifunctional Oxygen Performance. *Journal of Power and Energy Engineering*, **13**, 76-94.
https://doi.org/10.4236/jpee.2025.136005

Received: May 21, 2025
Accepted: June 27, 2025
Published: June 30, 2025

Abstract

Rechargeable zinc-air batteries (ZABs) represent a viable energy solution; however, the slow kinetics of the oxygen evolution reaction (OER) and the oxygen reduction reaction (ORR) severely hinder their commercial application, leading to a surge in research focused on the preparation of related catalysts. High-entropy materials possess unique physicochemical properties, while carbon nanofiber materials are ideal catalyst carriers. In this study, high-entropy carbon nanofiber materials HCNF/HEA were successfully prepared through electrospinning technology and high-temperature heat treatment. Zinc was used to create defects, and Mn, Fe, Co, La, and Gd were employed as stable structural elements. The lattice distortion effect of high-entropy materials generates local strain fields, forming abundant active sites; the "cocktail effect" optimizes the electronic structure through the synergistic effect between elements. Carbon nanofiber materials, due to their high specific surface area, good conductivity, and tunable porous structure, are ideal catalyst carriers. Electrochemical performance evaluations indicate that HCNF/HEA exhibits excellent bifunctional oxygen catalysis activity (with an overpotential of 1.65 V and a positive half-wave potential of 0.795 V). Additionally, the assembled zinc-air battery demonstrates outstanding device performance, including a high power density of 120.01 $mW \cdot cm^{-2}$, a specific capacity of 797.68 $mAh \cdot g^{-1}Zn$, and excellent stability over 240 hours, surpassing the commercial benchmark Pt/C-based zinc-air batteries.

Keywords

High-Entropy Materials, Carbon Nanofiber Materials, Oxygen Reduction Reaction, Zinc-Air Battery, Electrospinning Technology

1. Introduction

With the continuous rise in global energy demand and the exacerbation of greenhouse effects caused by the overuse of fossil fuels [1] [2], For the sustainable development of mankind, smart living, energy optimization, and the development of efficient and clean energy conversion and storage technologies have become major issues in the world [3]-[5]. Among various solutions, electrochemical energy devices such as proton exchange membrane fuel cells (with energy densities reaching 200 - 1000 Wh/kg) and zinc-air batteries (theoretical energy density of 1086 Wh/kg) have gained attention due to their high energy conversion efficiency (fuel cell efficiency can reach 60%) and environmental friendliness [6]. However, the performance of these devices is largely limited by the slow kinetics of the oxygen reduction reaction (ORR) and oxygen evolution reaction (OER). Therefore, developing efficient and stable bifunctional electrocatalysts for oxygen is crucial for improving the performance of these energy devices.

High-entropy materials, as emerging functional materials, exhibit unique physicochemical properties due to their multi-principal element characteristics (5 types of nearly equimolar elements) [7]-[9]. The high-entropy effect maximizes configurational entropy to reduce the system's Gibbs free energy, enhancing structural stability [10]; the lattice distortion effect generates local strain fields, creating a wealth of active sites [11]; the "cocktail effect" optimizes electronic structure through the synergistic interaction among elements [12]. These characteristics enable high-entropy materials to demonstrate mechanical properties, thermal stability, and catalytic activity that surpass traditional materials in the field of catalysis.

At the same time, carbon nanofiber materials have become ideal catalyst carriers due to their high specific surface area [13], good electrical conductivity [14], and adjustable pore structure [15]. Electrospinning technology can produce fibers with diameters ranging from 50 to 500 nm by controlling process parameters such as voltage, propulsion rate, and solution concentration. This nanoscale size effect can significantly increase the exposure of active sites [16]; in combination with subsequent treatments, it can form a gradient distribution of micropores (<2 nm), mesopores (2 - 50 nm), and macropores (>50 nm), which greatly enhances the specific surface area compared to traditional materials and significantly improves mass transfer rates and active site utilization [17]. Moreover, the rigid carbon nanofiber skeleton formed by high-temperature carbonization endows the material with excellent mechanical strength and physical-chemical stability (high-temperature resistance, corrosion resistance) [18] [19].

Based on the aforementioned advantages, researchers constructed a high-entropy/carbon fiber synergistic system through a composite strategy: embedding high-entropy nanoparticles into a nitrogen-doped carbon matrix, leveraging the triple synergistic effects of multi-active sites (high-entropy components), rapid electron conduction (carbon network), and charge redistribution (nitrogen doping) to potentially break through the performance limitations of commercial Pt/C (cost >

300 $/g) and RuO_2 (stability < 100 h). Recently, significant progress has been made in this area: Zhu *et al.* achieved the controllable preparation of high-entropy alloy nanoparticles (HEA NP) through electrospinning [20]. The Zhan team synthesized high-entropy one-dimensional nanowires HEA SNWs/C containing PtRuNiCoFeMo metals using a high-temperature oil bath; compared to commercial PtRu/C and Pt/C catalysts, HEA SNWs/C demonstrated high activity, enhanced stability, and good resistance to CO poisoning, showcasing excellent catalytic performance for the hydrogen oxidation reaction (HOR) [21]. Song et al. developed copper-based high-entropy nanofibers (Cu NPs) by loading metal precursors onto a carbon substrate using carbon thermal shock (CTS) technology. Theoretically, Cu NPs were shown to form numerous defect sites, possessing outstanding carbon dioxide reduction (CO_2 RR) performance [22]. Yao *et al.* improved the CTS process by loading metal salt precursors onto conductive carbon carriers, rapidly thermally shocking them in an Ar-filled glove box, resulting in the formation of a high concentration of nanoparticles on the carbon surface, and developed pentanary HEA-NPs as ammonia oxidation catalysts (ASC), achieving nearly 100% conversion rate and >99% selectivity for nitrogen oxides [23].

This study aims to explore the synthesis methods of high-entropy carbon nanofiber materials and systematically investigate their catalytic performance in oxygen reduction and oxygen evolution reactions. High-entropy carbon nanofiber materials HCNF/HEA were successfully prepared using electrospinning technology and high-temperature heat treatment processes. The structure and composition of the materials were analyzed using various characterization methods, and their catalytic performance was evaluated through electrochemical testing. This study not only provides new insights for the development of novel and efficient bifunctional oxygen electrocatalysts but also holds significant importance for promoting the application of high-entropy materials in the energy field.

2. Experimental Section: Synthesis and Characterization

2.1. Synthesis of HCNF/HEA and CNF/FeN

This study utilizes electrospinning technology combined with high-temperature heat treatment processes to prepare high-entropy carbon nanofiber materials. First, six types of transition metal salts were weighed: 0.5 mmol of $MnCl_2{\cdot}4H_2O$, $Fe(NO_3)_3{\cdot}9H_2O$, $Co(NO_3)_2{\cdot}6H_2O$, $La(NO_3)_3{\cdot}6H_2O$, $Gd(NO_3)_3{\cdot}6H_2O$, and 2 mmol of $Zn(NO_3)_2{\cdot}6H_2O$ into a beaker, then 1.5 g of polyacrylonitrile (PAN) dissolved in 22 g of N,N-dimethylformamide (DMF) was added to the beaker. The solution was stirred at 1000 rpm for 8 hours at room temperature to prepare the spinning precursor solution. Subsequently, the spinning solution was extracted with a syringe and electrospun using an electrospinning device at a voltage of 15 kV, with a feeding rate set at 0.3 ml/h, and the syringe was positioned 18 cm from the collector, yielding a precursor nanofiber membrane. The precursor fiber membrane was pre-oxidized in an air atmosphere at a heating rate of 2˚C/min to 230˚C for 3 hours, and then transferred to a tubular furnace for carbonization in an argon

atmosphere at 1000˚C for 3 hours, followed by natural cooling to obtain the high-entropy carbon nanofiber material HCNF/HEA. The precursor prepared without adding $MnCl_2{\cdot}4H_2O$, Gd $(NO_3)_3{\cdot}6H_2O$, but only with the corresponding concentrations of $Fe(NO_3)_3{\cdot}9H_2O$, $Co(NO_3)_2{\cdot}6H_2O$, $Zn(NO_3)_2{\cdot}6H_2O$, and $La(NO_3)_3{\cdot}6H_2O$, underwent the same processes of spinning, pre-oxidation, and carbonization, resulting in the material named CNF/FeN.

2.2. Materials Characterization

X-ray diffraction (XRD) characterization was performed using a D8 Advance X-ray diffractometer equipped with a non-monochromated Cu Kα X-ray source (λ = 1.054056 Å). Transmission electron microscopy (TEM) was used to characterize the morphology and microstructure of the synthetic materials, and energy dispersive X-ray spectroscopy (EDS) was performed to analyze the element distribution, both of which were collected using JEOL JEM 2100 F instrument from Japan. The specific surface area and pore size distribution were determined from nitrogen adsorption/desorption measurements using a JWGB INSTRUMENTS BK112 physical adsorption analyzer, based on the Brunauer-Emmett-Teller (BET) multipoint method and the Barret-Joyner-Halenda (BJH) model. Raman measurement was carried out using a LabRAM HR Evolution Raman spectrometer from HORIBA FRANCE, with a laser source wavelength of 532 nm. The chemical valence structure of the elements on the surface of the material was analyzed by X-ray photoelectron spectroscopy (XPS) with a Thermo Fisher Scientific K-Alpha instrument from the United States.

2.3. Electrochemical Measurements

All electrochemical performance data were obtained using a rotating disk electrode (RDE, PINE Research Instrumentation) with a CHI760E electrochemical workstation at 25˚C, utilizing a thermostatic water bath. All tests were carried out using a three-electrode system, with platinum sheet electrodes serving as the counter electrode and Hg/HgO (1 M KOH) as the reference electrode. Rotating disk electrodes (RDE, diameter = 5 mm) were employed as the working electrodes. To create a well-distributed catalyst ink, 5 mg of the electrocatalyst sample was ground for 1 hour and then dispersed in 480 μL of ethanol and 20 μL of 5 wt% Nafion solution (Dupont) via ultrasonic dispersion for at least 30 minutes. A 20 μL drop of this mixture was then applied onto the working electrode and allowed to dry naturally, ensuring that the catalyst loading was 1.018 mg cm^{-2}. For comparison, a commercial 20 wt% Pt/C catalyst ink was prepared using the same procedure described above.

Before conducting the tests, a 0.1 M KOH solution should be saturated with N_2/O_2. LSV was recorded in the N_2/O_2-saturated 0.1 M KOH solution at a rotation speed of 1600 rpm at 5 $mV{\cdot}s^{-1}$. The electrochemically active surface area (ECSA) was determined by estimating electrochemical double-layer capacitances (C_{dl}) using cyclic voltammograms in a non-faradaic region (1.07 - 1.17 V) at various scan

rates (10, 20, 30, 40, 50 and 60 $mV \cdot s^{-1}$). The capacitive currents, represented as $\Delta J/2$ (where $\Delta J = J_a - J_c$, with J_a and J_c denoting the anodic and cathodic current densities at 1.12 V vs. RHE, respectively), were plotted against the scan rate and fitted to a linear regression. The slope of this linear fit corresponds to C_{dl}. All LSV curves were obtained by subtracting the capacitive currents in the N_2 saturated electrolyte. All potentials derived from the RDE/RRDE tests in 0.1 M KOH were converted to RHE potentials by the equation $E_{RHE} = E_{Hg/HgO} + 0.8676$ V, based on the calibration results, and were corrected with 80% iR-compensation. Tafel plot was created by fitting the voltage as the vertical axis and the logarithm of the current density as the horizontal axis. The kinetic current density (J_k) and the number of electrons transferred (n) were calculated according to the Koutecky-Levich equations given below:

$$\frac{1}{J} = \frac{1}{J_L} + \frac{1}{J_k} = \frac{1}{B\omega^{1/2}} + \frac{1}{J_k} \tag{1}$$

$$B = 0.62nFC_0 \left(D_0\right)^{2/3} v^{-1/6} \tag{2}$$

where J and J_k represent the measured current density and the kinetic current density, respectively. ω is the electrode rotation speed, and B can be determined from the slope of the K-L plots. The variable n indicates the number of electrons transferred per oxygen molecule, F is the Faraday constant (96485 $C \cdot mol^{-1}$), D_0 is the diffusion coefficient of O_2 (1.9×10^{-5} $cm^2\ s^{-1}$), V is the kinetic viscosity (0.01 $cm^2 \cdot s^{-1}$), and C_0 is the concentration of O_2 (1.2×10^{-6} $mol \cdot cm^{-3}$). Electrochemical impedance spectroscopy (EIS) measurements were conducted at open-circuit voltages across a frequency range of 10^2 - 10^6 Hz. Stability tests and anti-toxicity measurements were carried out using long-term chronoamperometry of −0.25 V (vs. RHE).

2.4. Assembly and Test of Zn-Air Batteries

Zn-air batteries were fabricated and evaluated in an atmospheric environment at room temperature. A polished Zn foil with a thickness of 0.2 mm was employed as the anode. The air electrode was prepared by drop-casting a catalyst ink onto hydrophobic carbon paper (Fuel Cell Store, effective area = 2 cm^{-2}), yielding a catalyst loading of 0.8 $mg \cdot cm^{-2}$. A waterproof and breathable membrane, along with Ni foam, served as the gas diffusion layer (GDL) and current collectors, respectively. The electrolyte consisted of 6 M KOH aqueous solutions. The open circuit potential and discharge polarization curve were recorded using LSV at a scan rate of 5 $mV \cdot s^{-1}$ on a CHI760E electrochemical workstation. For comparison, a commercial Pt/C catalyst was prepared using the same procedure to fabricate an additional Zn-air battery. The charge-discharge cycle stability of the Zn-air batteries was evaluated using Landt Instruments. The specific capacity ($mAh \cdot g^{-1}$) was calculated using the following equations:

$$\text{Specific capacity} = \frac{\text{discharge current} \times \text{working time}}{\text{mass of consumed zinc}} \tag{3}$$

3. Results and Discussion

3.1. Preparation and Structural Characterization

In this study, high-entropy carbon nanofibers (HCNF/HEA) were prepared by electrospinning-high-temperature pyrolysis. Figure 1 is a schematic diagram of its preparation, briefly, six transition metal salts (Mn, Fe, Co, La, Gd and Zn) are dissolved in DMF together with polyacrylonitrile, and the precursor solution is formed by magnetic stirring. Homogeneous nanofiber membranes were obtained by electrospinning, followed by a two-step heat treatment: pre-oxidation at 230˚C for 3 hours and carbonization at 1000˚C for 3 hours, and finally HCNF/HEA, the target material for high-entropy CNFs. The lattice distortion effect produces a local strain field, forming abundant active sites. The "cocktail effect" optimizes the electronic structure through the synergy between elements. The rigid carbon nanofiber skeleton formed by high-temperature carbonization gives the material excellent mechanical strength and physicochemical stability.

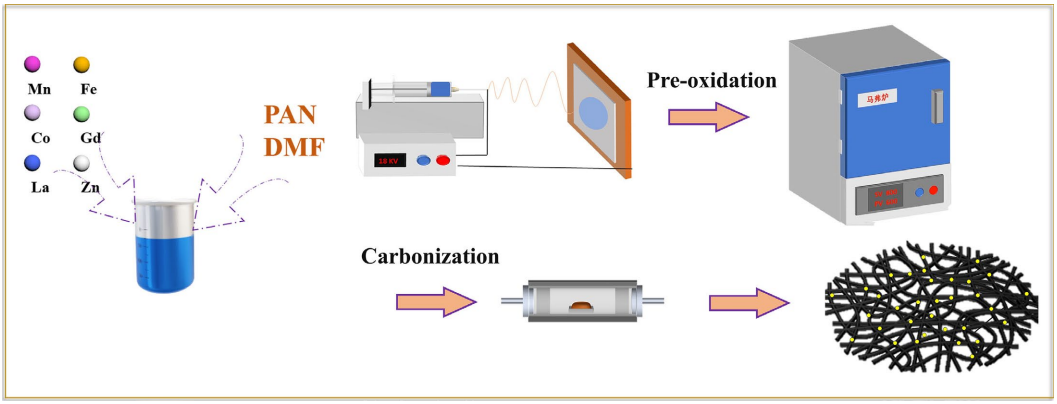

Figure 1. Schematic diagram of the preparation of HCNF/HEA.

The prepared catalyst material HCNF/HEA was subjected to XRD testing (Figure 2). Through X-ray diffraction (XRD) analysis, it was found that the resulting material exhibited sharp diffraction peaks of metals or metal carbides, indicating that metal elements may be present in the carbon matrix. The XRD spectrum of HCNF/HEA can be matched with JCPDS cards, which correspond to the metallic composite crystal structures of Co_3Fe_7 JCPDS#48-1817, La_4Co_3 JCPDS#21-0262, and $FeGdC_2$ JCPDS50-0992 [24]. Compared to the standard spectrum of FeNi alloy (PDF#47-1417), the diffraction peaks of HCNF/HEA exhibit slight shifts due to lattice distortion caused by the introduction of foreign atoms and the resulting high entropy.

Transmission electron microscopy (TEM) observations show that the HCNF/HEA materials maintain a tubular nanofiber structure, with a fiber diameter of about 100 nm. A large number of alloy nanoparticles are densely and uniformly anchored in the CNFs (Figure 3(a), Figure 3(b), and Figure 3(c)) also showing clearly visible lattice fringes, which further reveal the crystal structure of the HEAs. The scanning transmission electron microscopy energy dispersive X-ray (STEM-EDS) elemental mapping image (Figure 3(d)) reveals that HCNF/HEA is

rich in N-C structure. The doping of nitrogen and the formation of metal-nitrogen coordination structures are believed to contribute to enhancing the electrocatalytic performance of the materials [25]. The elements Mn, Fe, Co, La, Gd, and Zn are successfully distributed throughout the carbon nanofibers, and the elements Fe, Co, Ni, La, Gd, and Zn aggregate to form high-entropy nanohybrid clusters, which are widely distributed within the CNFs. The lattice distortion and cocktail effect inherent in high-entropy alloys enable the catalyst to exhibit comprehensive performance far exceeding that of traditional alloys [26].

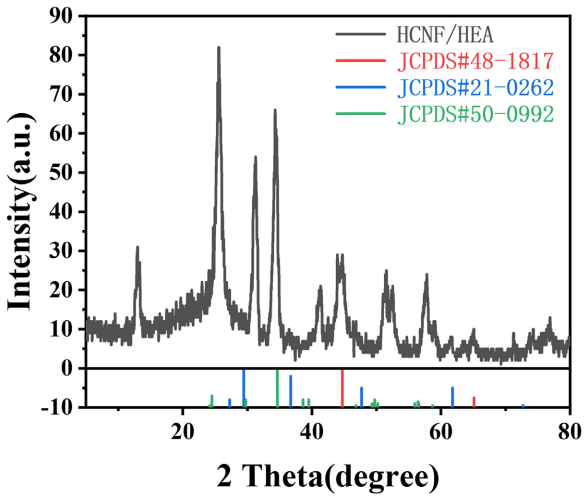

Figure 2. XRD analysis of HCNF/HEA.

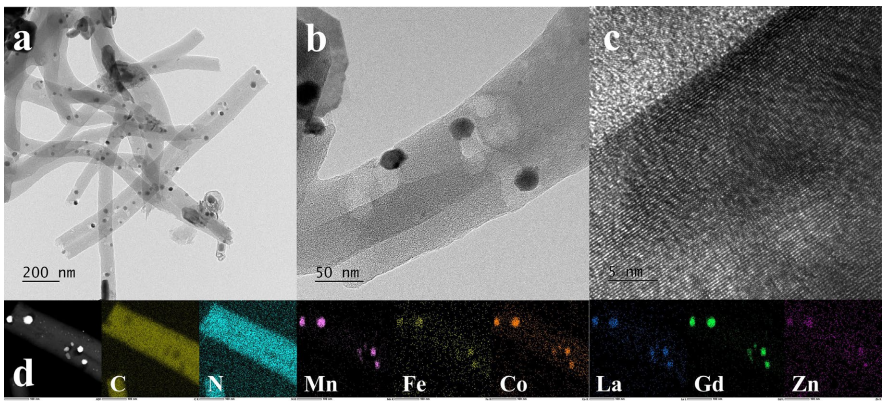

Figure 3. (a)-(c) TEM image; (d) EDS element mapping image of HCNF/HEA.

The pore structure has a significant impact on ion transport, and adsorption-desorption experiments were conducted on the materials. Figure 4(a) shows the nitrogen adsorption-desorption curve and pore size distribution of HCNF/HEA. At lower relative pressures, the amount of adsorption exhibits a plateau, indicating the presence of micropores [27]. As the relative pressure increases, the appearance of a hysteresis loop is observed, and when the relative pressure approaches 1, the amount of adsorption increases significantly. These features indicate the simultaneous presence of mesopores and macropores in the material [28]. The

BET calculation based on N_2 gives a specific surface area of 564.506 $m^2 \cdot g^{-1}$, and the appropriate porous structure in the carbon fiber endows it with a large specific surface area. This characteristic allows the electrolyte to penetrate sufficiently, accelerating electron transfer and the embedding/releasing of oxygen species, which endows HCNF/HEA with excellent ORROER performance [29]. The Raman spectrum of the HCNF/HEA material is shown in **Figure 4(b)**. In the Raman spectra of carbon materials, the D peak and G peak are two significant characteristic marks. The D peak indicates the presence of amorphous carbon or structural defects in the material, while the G peak reflects the characteristics of the graphite structure [30] [31]. The D and G peaks are located at 1365 cm^{-1} and 1587 cm^{-1}, respectively. The intensity ratio ID/IG of the HCNF/HEA material is 0.885, indicating that the carbon materials in the carbon fiber of the HCNF/HEA composite have developed a sufficient amount of defects and a high degree of graphitization at high temperatures. The redshift and blueshift of the D and G peaks can be attributed to the functional groups formed by the multi-metal.

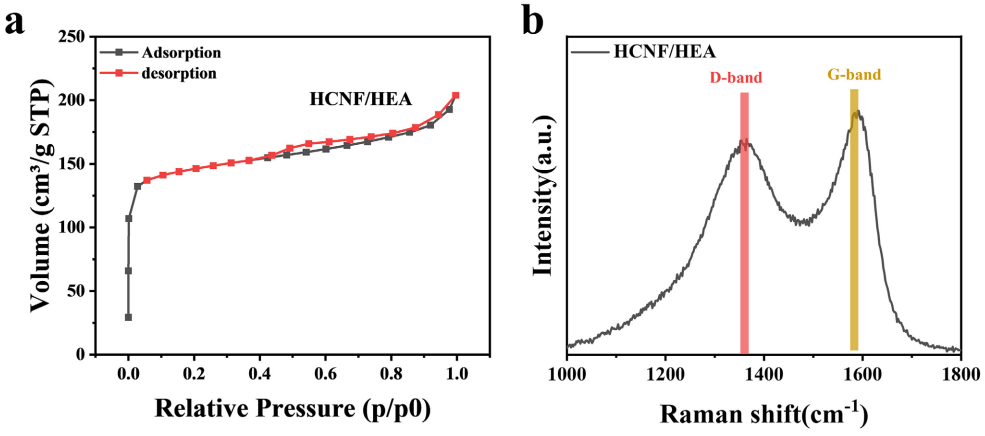

Figure 4. (a) Nitrogen adsorption/desorption curves; (b) Raman spectra of HCNF/HEA.

XPS analysis is used to determine the elemental composition of the sample surface and its relative contents. As shown in **Figure 5**, within the binding energy range of 0 - 1200 eV, the sample mainly contains characteristic peaks of three elements: C, O, and N, corresponding to the electronic orbital signals of C 1s (~284.8 eV), O 1 s (~532 eV), and N 1 s (~401.5 eV). The detection of signals for metal elements such as Ld, Co, Mn, Fe, and Co in the XPS full spectrum indicates that the preparation process successfully introduced various metal components, further confirming that the material achieved high-entropy synthesis (**Figure 5(a)**). The Gaussian-Lorentzian peak fitting of the C 1s spectrum (**Figure 5(b)**) reveals three characteristic peaks: 284.8 eV corresponding to sp^2 hybridized carbon (C=C/C–C) reflecting graphene-like carbon framework structure; 285.7 eV attributed to C–N/C=N bonds, indicating that the incorporation of nitrogen in HCNF/HEA enriches the N-C structure; and 289.0 eV corresponding to carboxylic acid groups (O–C=O), typically located at edge defect sites of carbon materials. The oxygen-containing functional groups in the C 1s spectrum suggest that the material

surface has significant oxidative characteristics, which is beneficial for enhancing hydrophilicity and chemical reactivity [32]. The peak fitting results of the O 1s spectrum (**Figure 5(c)**) show three main components: the peak at 529.8 eV corresponds to lattice oxygen of metal oxides; the peak at 531.9 eV represents adsorbed water or carboxylic acid oxygen (C=O); and the peak at 533 eV can be attributed to carbon and hydroxyl bond sites (−OH). The high ratio of C−O (533 eV) and O−C=O (531.9 eV) components further validates the presence of oxygen functional groups in the C 1s spectrum [33]. **Figure 5(d)** displays the N 1s spectrum of HCNF/HEA, which was fitted to obtain three forms of nitrogen doping: 398.5 eV: pyridinic nitrogen (Pyridinic-N), contributing electrons to the π-conjugated system; 401.0 eV: graphitic nitrogen (Graphitic-N), which can improve the conductivity of the material; and the peak at 404.9 eV can be attributed to oxidized nitrogen species. The role of pyridinic nitrogen can significantly enhance the catalytic performance of the material, while the presence of graphitic nitrogen helps maintain the conductive network [34]. HCNF/HEA material is carbon-based, forming a sp^2/sp^3 mixed hybrid structure, with a surface rich in hydroxyl and carboxyl oxygen-containing functional groups, which has an important impact on the material's performance. For example, pyridinic nitrogen and graphitic nitrogen can serve as active sites and conductive channels, respectively, to enhance the conductivity of the catalyst [35]; the synergistic effect of C=O and pyrrolic nitrogen may enhance the electrocatalytic activity [36]; and the rich oxygen-containing functional groups help to improve the dispersion of the material in aqueous systems [37].

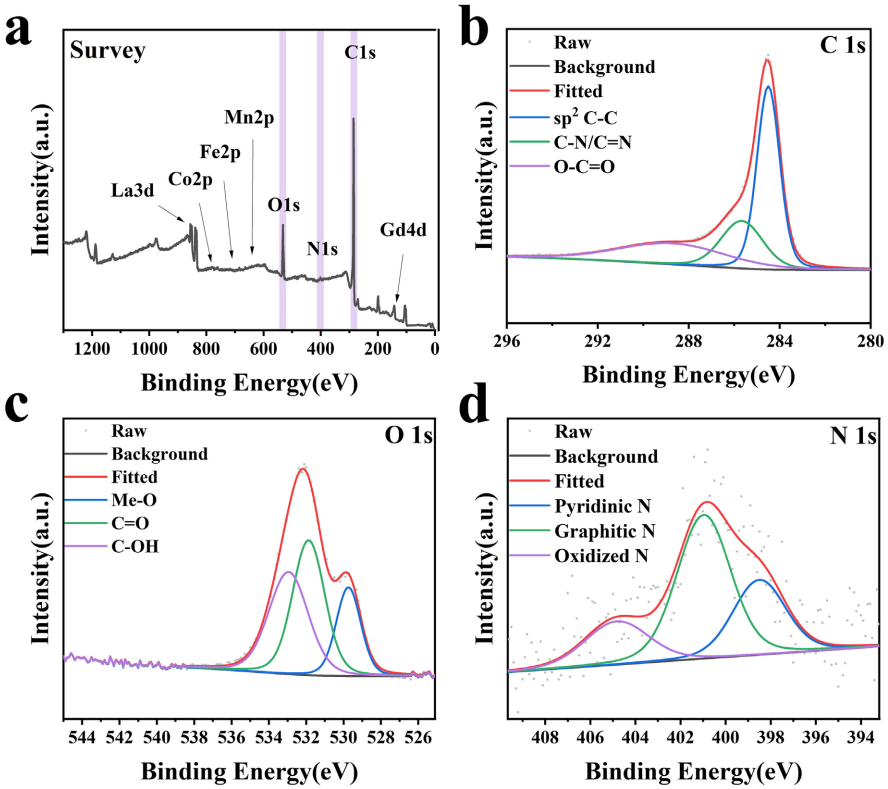

Figure 5. (a) XPS total spectrum of HCNF/HEA and XPS plots of (b) C 1s, (c) O 1s, (d) N 1s.

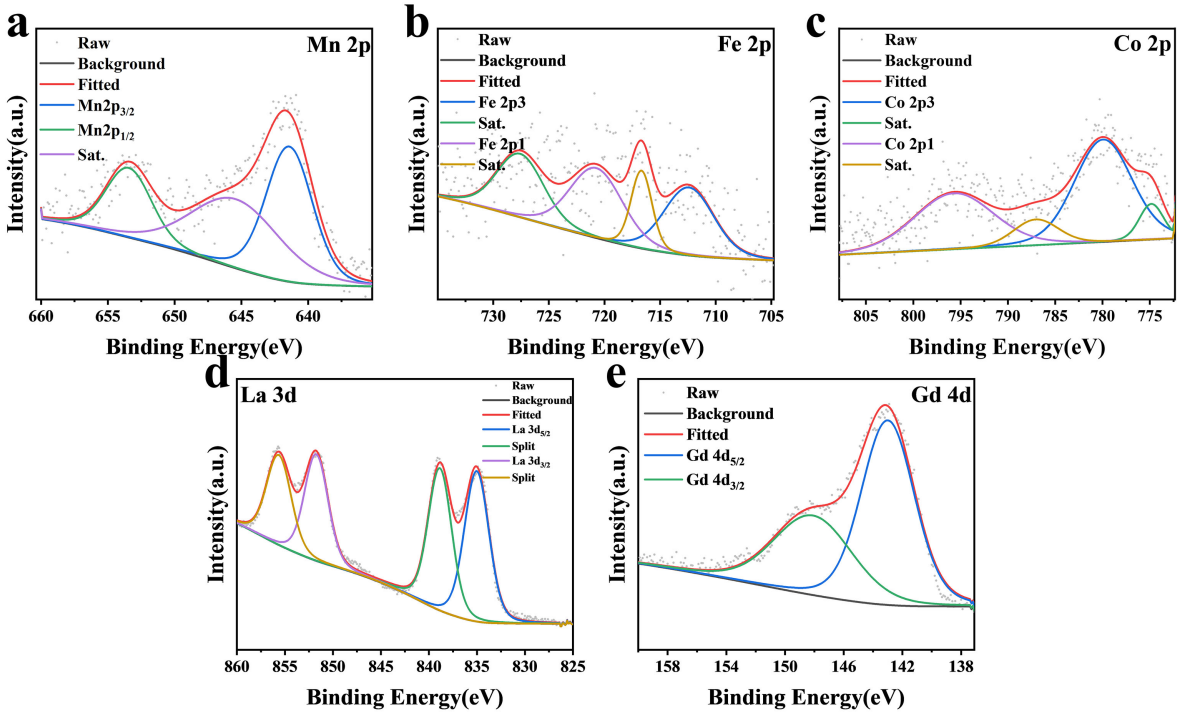

Figure 6. XPS spectra of (a) Mn 2p, (b) Fe 2p, (c) Co 2p, (d) La 3d and (e) Gd 4d of HCNF/HEA.

Through peak fitting, the Mn 2p spectrum of HCNF/HEA (**Figure 6(a)**) presents a typical double peak structure (Mn $2p_{3/2}$ at 641.5 eV and Mn $2p_{1/2}$ at 653.6 eV), indicating the presence of Mn^{2+}. There are partially redox-active sites on the material's surface, possibly related to the electron transfer with the carbon matrix. Additionally, satellite peaks were observed in the 646 eV range, further supporting the Mn^{2+} characteristics [38]. The Fe 2p spectrum (**Figure 6(b)**) displays the main peaks of $2p_{3/2}$ and $2p_{1/2}$ located at 712.6 eV and 721.48 eV, with satellite peaks for Fe observed at 727.7 eV and 716.7 eV, consistent with Fe^{3+} characteristics. The interaction of Fe with metals like Mn, Co, etc., forms a multi-metallic synergistic system that enhances the material's magnetic or electrocatalytic activity [39] [40]. The Co 2p spectrum in **Figure 6(c)** shows the main peaks of $2p_{3/2}$ and $2p_{1/2}$ located at 780 eV and 795.7 eV, and satellite peaks are present at 786.9 eV and 774.8 eV [41]. The La 3d spectrum (**Figure 6(d)**) displays typical double peak splitting ($3d_{5/2}$ and $3d_{3/2}$), with split peaks located at 853.6 eV and 836.6 eV, corresponding to La $3d_{5/2}$ and La $3d_{3/2}$, respectively. Its high electronegativity may regulate the electronic structure of the carbon fiber surface through electron modulation effects, enhancing its adsorption capacity for specific molecules (like O_2). This is also one of the reasons for selecting La and Gd elements in this paper [42] [43]. The Gd 4d spectrum (**Figure 6(e)**) shows broad peak characteristics due to weak spin-orbit coupling. Peak fitting indicates a Gd $4d_{5/2}$ peak at 143.1 eV and a Gd $4d_{3/2}$ peak at 148.3 eV. The interface of gadolinium with the carbon matrix may introduce local magnetic moments through its 4f electronic characteristics, synergistically enhancing the material's magnetic responsiveness with Fe and Co. Moreover, the

high polarizability of Gd^{3+} could optimize the adsorption energy of reaction intermediates by surface charge rearrangement [44]. The low detection of Zn in XPS may be due to the high-temperature evaporation of free Zn species on the surface during carbonization [45]. The analysis of XPS for Mn 2p, Fe 2p, Co 2p, La 3d, and Gd 4d reveals the chemical states and synergistic mechanisms of multi-metal elements in high-entropy carbon fibers, providing a theoretical basis for designing high-performance high-entropy carbon-based materials.

3.2. Electrochemical Analysis

To evaluate the catalytic performance of high-entropy CNF materials, electrochemical analysis was conducted comparing HCNF/HEA with CHF/FeN materials. CV cycles were tested under O_2 and N_2 atmospheres in the range of 0.1 V to 1.2 V (vs. RHE) (**Figure 7(a)**). Under nitrogen conditions, there were no significant redox peaks, while in oxygen, both HCNF/HEA and CHF/FeN exhibited distinct redox peaks, indicating their efficient redox activity. The multi-element synergistic effect of HEA increased the density of active sites, promoting O_2 adsorption and dissociation. The Nyquist plot in **Figure 7(b)** shows that the charge transfer resistance (Rct) of HCNF/HEA is 38 Ω, lower than that of CHF/FeN (42.5 Ω), indicating that HCNF/HEA has a faster electron transport rate.

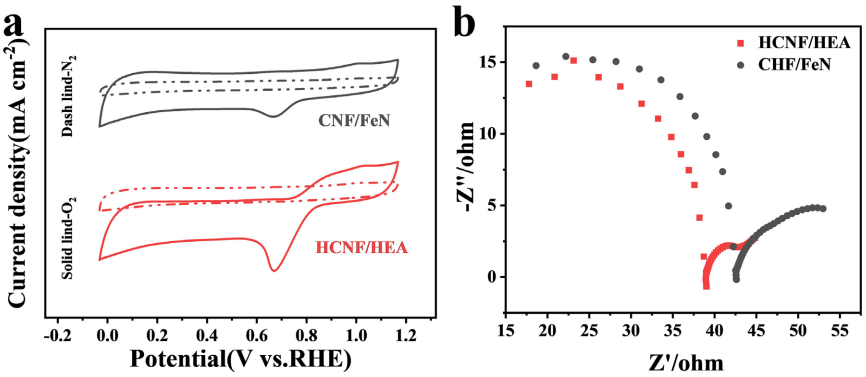

Figure 7. (a) CV cyclic test plots of HCNF/HEA and CHF/FeN in O_2 and N_2 atmospheres, and (b) their impedance measurements.

By scanning the voltage of the illegal Faraday region (1.06 - 1.16 V vs. RHE) at different scan rates, the double-layer capacitance and electrochemically active surface area can be calculated (**Figure 8**). **Figure 8(a)** and **Figure 8(b)** show the CV tests at different scan rates. It can be seen that HCNF/HEA and CHF/FeN show slight differences, which may be caused by electrode polarization. Based on the test results, the difference in current density at the center of the image at different scan rates is obtained, and it is fitted that the Cdl of HCNF/HEA is 23.8 $mF \cdot cm^{-2}$, which is better than CHF/FeN's 18.1 $mF \cdot cm^{-2}$ (**Figure 8(c)** and **Figure 8(d)**). The multi-level pore structure and surface roughness significantly enhance the density of active sites, and the high Cdl value of HEA also indicates that the multiple elements provide exposed active edge sites.

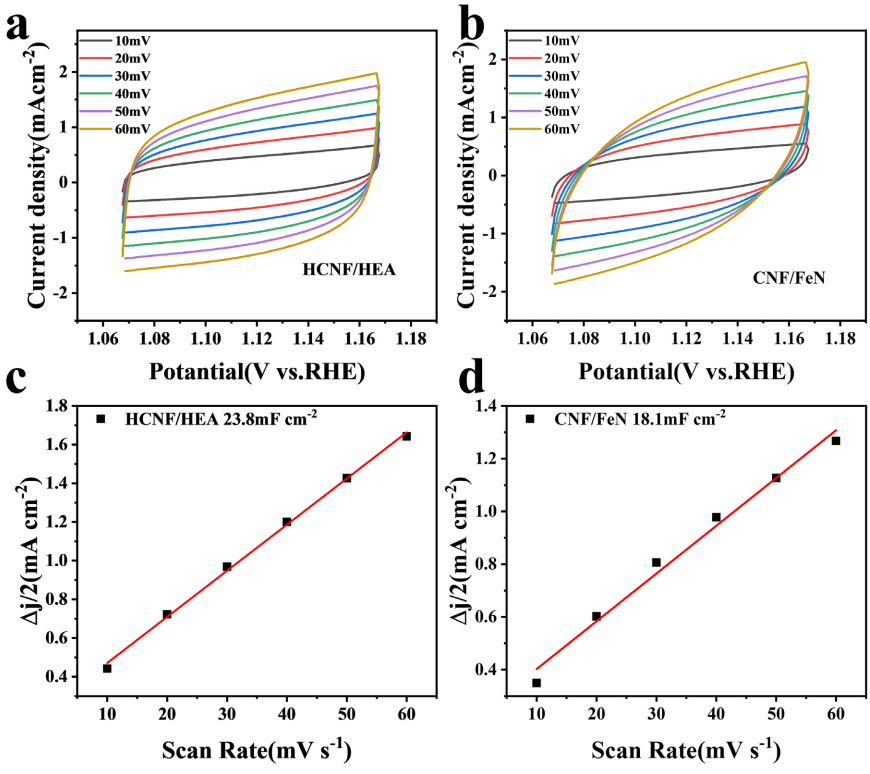

Figure 8. (a) (b) CV tests in the non-faradaic region at different scan rates; (c) (d) Double-layer capacitance calculations for HCNF/HEA and CNF/FeN.

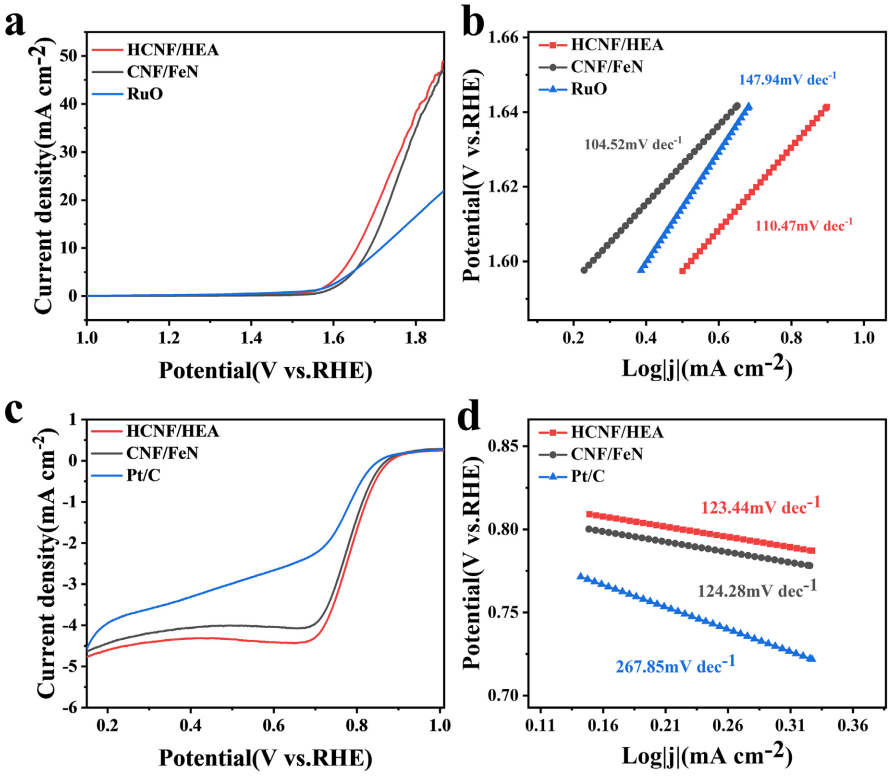

Figure 9. Electrochemical ability tests for HCNF/HEA, CHF/FeN, and Pt/C. (a) LSV test for OER; (b) corresponding taffel slope; (c) LSV test for ORR; (d) corresponding Tafel slope.

In order to visually observe the catalytic activity of high-entropy materials HCNF/HEA, LSV tests and Tafel slope fittings were conducted (Figure 9). OER tests (Figure 9(a) and Figure 9(b)) indicate that high-entropy CNFs materials possess good OER catalytic activity, with the corresponding voltages for HCNF/HEA, CHF/FeN, and RuO at a current density of 10mA·cm^{-2} being 1.65 V, 1.68 V, and 1.71 V, respectively. Additionally, the Tafel slopes of the high-entropy material catalysts at 110.47 mV· dec^{-1} and 104.52 mV·dec^{-1} are both superior to that of the commercial RuO catalyst at 147.94 mV·dec^{-1}. The testing system for ORR (Figure 9(c) and Figure 9(d)) shows that the half-wave voltages for HCNF/HEA and CHF/FeN are 0.795 V and 0.787 V, respectively, which are higher than the 0.779 V of the commercial Pt/C catalyst. The ORR Tafel slopes of high-entropy CNFs materials also perform well, with 123.44 mV·dec^{-1} for HCNF/HEA and 124.28 mV·dec^{-1} for CHF/FeN, both of which are better than the 267.85 mV·dec^{-1} of the Pt/C catalyst.

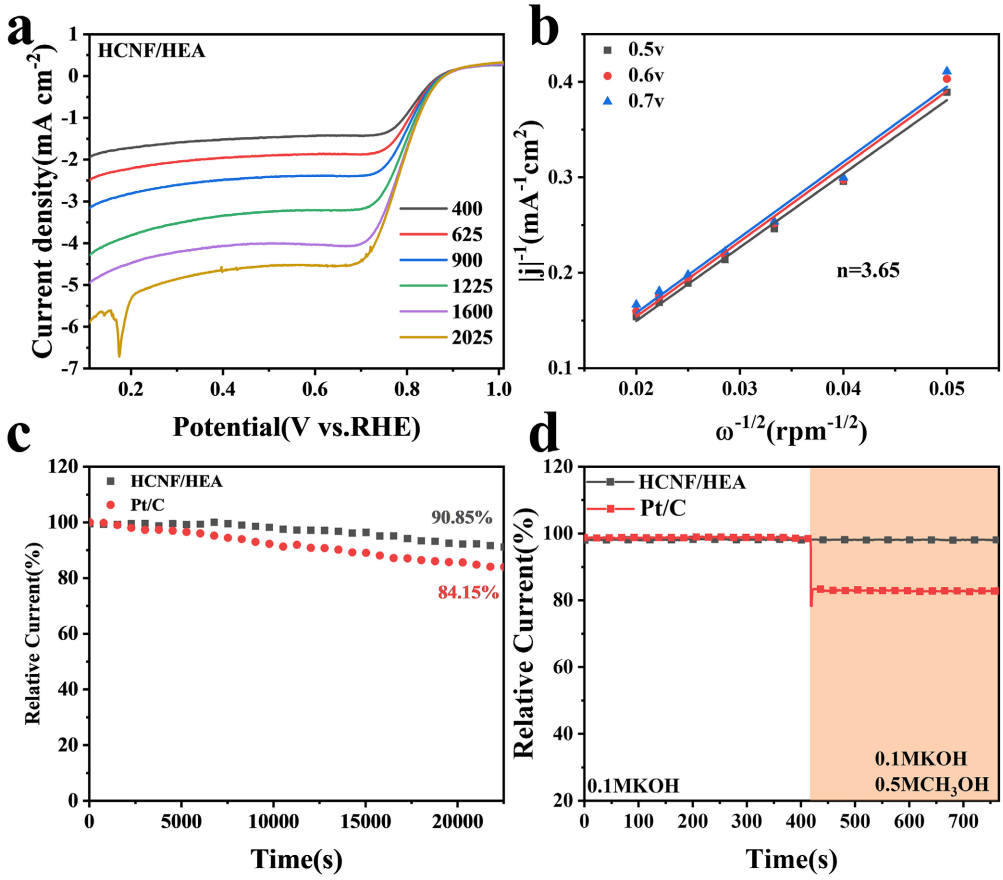

Figure 10. Electron transfer and stability tests for HCNF/HEA (a) LSV tests for ORR at different speeds; (b) corresponding K-L calculations; (c) i-t chronoelectric current test; (d) methanol resistance toxicity test.

In order to investigate the four-electron reaction capability of HCNF/HEA, LSV tests for ORR were conducted at different rotation speeds. Based on the data measured from Figure 10(a), the rotation speed and current density were extracted to

plot the K-L calculation line in Figure 10(b). The calculation result indicates that the electron transfer number n = 3.65 for HCNF/HEA, demonstrating a sufficiently high four-electron response performance. To examine the stability of HCNF/HEA, we carried out a time-current (i-t) test (Figure 10(c)). The results show that HCNF/HEA maintained a current response for 25,000 s at open-circuit voltage, and the relative current was 90.85% of the original value, indicating low loss; in contrast, the current for Pt/C showed a significant drop to 84.15% of its original value. To study the catalyst's anti-poisoning performance, methanol was added during the timed current test to observe changes in performance. The results in Figure 10(d) show that adding methanol at 400 s did not cause any significant change in the i-t curve for HCNF/HEA. In stark contrast, the i-t curve for the commercial Pt/C catalyst displayed a significant negative shift compared to its initial value under the same test conditions, demonstrating the excellent anti-poisoning stability of HCNF/HEA.

3.3. Zinc-Air Battery Test

In order to further study the practical application of the target catalyst in zinc-air batteries (ZAB), it was assembled into an aqueous zinc-air battery (Figure 11(a)). It can be observed that the open circuit voltage of the HCNF/HEA-based ZAB stabilized at 1.38 V, close to that of the commercial Pt/C-based ZAB (1.40 V) (Figure 11(b)). To test the discharge specific capacity, the assembled zinc-air batteries underwent constant current discharge tests until the battery could no longer operate (Figure 11(c)). The results showed that the discharge specific capacity of the HCNF/HEA ZAB was 797.68 $mAh \cdot g^{-1}$, higher than the 767.60 $mAh \cdot g^{-1}$ of the commercial Pt/C-based ZAB. This difference may be due to battery polarization or the occurrence of side reactions, which also indirectly indicates the corrosion resistance of the HCNF/HEA. In addition, the charge-discharge curves of the zinc-air batteries were measured, revealing that the ZAB assembled with HCNF/HEA exhibited good charge-discharge efficiency compared to the Pt/C catalyst-based ZAB. The power density curve was obtained from the ZAB discharge curve (Figure 11(d)). The maximum power density of the HCNF/HEA-based ZAB was 120.01 $mW \cdot cm^{-2}$, approaching the peak power density (124.62 $mW \cdot cm^{-2}$) of the commercial Pt/C ZAB. The good performance of HCNF/HEA can be attributed to the high entropy effect brought by the high-entropy alloy and the excellent protection and conductivity of graphite carbon fibers.

Considering the excellent corrosion resistance and stability of HCNF/HEA, it was loaded onto a ZAB and then tested on a new power battery tester to assess its long-term cycling stability performance (Figure 12). The results showed that under a current density of 10 $mA \cdot cm^{-2}$ and a 10-minute charge-discharge cycle, the voltage range of the HCNF/HEA-based ZAB remained stable between 1 - 2.3 V, cycling stably for 240 hours without significant degradation. In contrast, the back-and-forth potential of the Pt/C-based ZAB sharply increased after about 2 hours, and after approximately 50 hours, the testing machine issued an alarm, which is

likely due to the battery being corroded by the catalyst. The overall robust performance of the ZAB indicates that HCNF/HEA holds significant potential for practical applications.

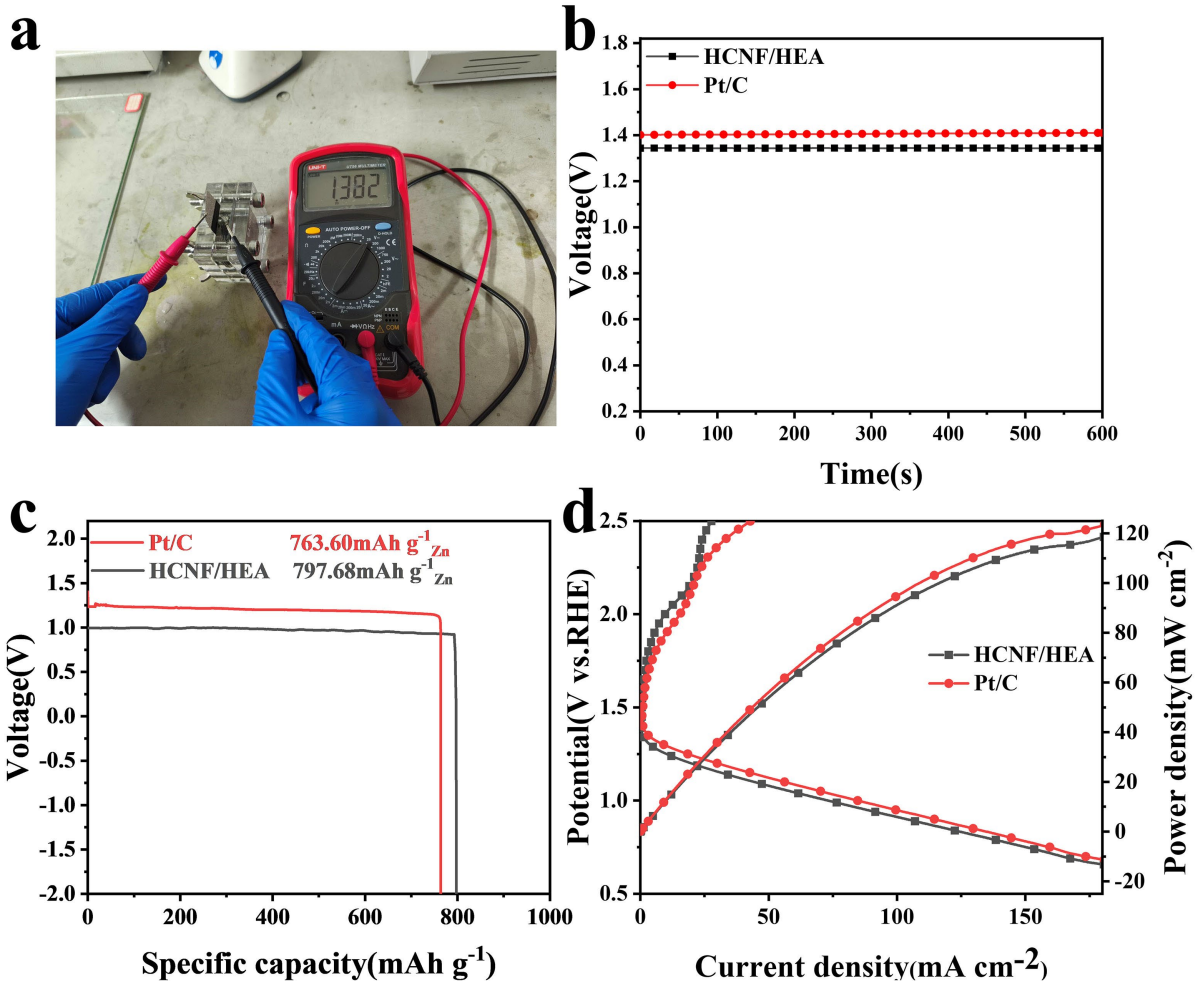

Figure 11. (a) Physical photos of HCNF/HEA-based ZAB open circuit voltage; (b) OCP test chart; (c) discharge specific capacity test; (d) charge-discharge polarization curve and power density curve of HCNF/HEA and Pt/C-based ZAB.

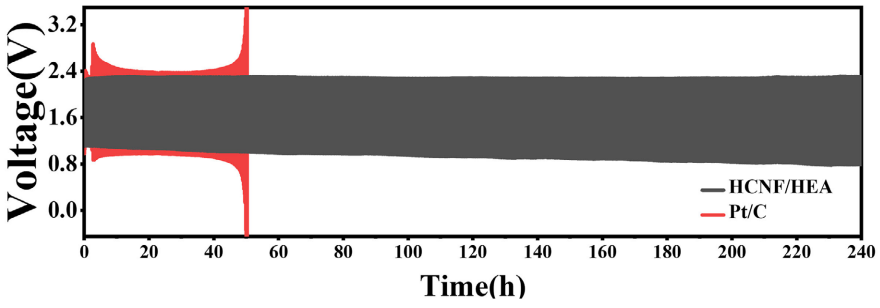

Figure 12. Long-cycle voltage curve of a ZAB loaded with HCNF/HEA and Pt/C.

4. Conclusion

In this work, an electrospinning-pyrolysis strategy was established to synthesize

Mn/Fe/Co/La/Gd high-entropy carbon nanofibers (HCNF/HEA), in which Zn-induced defect engineering and polymetallic synergistic effects jointly enhanced bifunctional oxygen electrocatalysis. Lattice distortion and the "cocktail effect" optimize the electronic structure, while the multi-stage carbon framework facilitates mass/charge transfer, enabling superior ORR/OER activity and zinc-air battery performance. Despite the encouraging results, there are still a number of issues that merit further study. For example, a 240-hour stability test indicates stability, but long runs (>500 hours) may reveal metal leaching or carbon corrosion. At the same time, the optimal proportion of metal elements is also worth studying; Finally, mechanical stability under bending stress should also be considered. This study validates HCNF/HEA as a high-performance, cost-effective oxygen-electrocatalytic catalyst. Addressing these limitations will provide a new idea for the development of efficient and stable bifunctional oxygen electrocatalysts to accelerate the deployment of zinc-air batteries in grid-scale renewable energy storage.

Funding

This research was financially supported by National Natural Science Foundation of China (No. 12164014), Guangxi Natural Science Foundation (No. 2022GXNSFAA035551).

Conflicts of Interest

The author declares no conflicts of interest regarding the publication of this paper.

References

[1] Coppez, G., Chowdhury, S. and Chowdhury, S.P. (2010) Impacts of Energy Storage in Distributed Power Generation: A Review. 2010 *International Conference on Power System Technology*, Zhejiang, 24-28 October 2010, 1-7. https://doi.org/10.1109/powercon.2010.5666075

[2] Icer, K., Rahman, S. and Adhikari, K. (2024) Autoregressive Modeling of Time Series in Renewable Energy Systems. 2024 *IEEE* 15*th Annual Ubiquitous Computing, Electronics & Mobile Communication Conference* (*UEMCON*), Yorktown Heights, 17-19 October 2024, 372-378. https://doi.org/10.1109/uemcon62879.2024.10754746

[3] Li, G., Zhang, J. and Yang, C. (2025) Recent Progress and Prospects of Hydrothermal Flames for Efficient and Clean Energy Conversion. *Journal of Cleaner Production*, **497**, Article ID: 145170. https://doi.org/10.1016/j.jclepro.2025.145170

[4] Reza Habib, A.K.M.R., Alam, M.M. and Islam, M.R. (2021) Design of a Mobile Aeration System for Aquaculture and Proof of Concept. 2021 *International Conference on Computer, Communication, Chemical, Materials and Electronic Engineering* (*IC4ME2*), Rajshahi, 26-27 December 2021, 1-4. https://doi.org/10.1109/ic4me253898.2021.9768594

[5] Luo, J. (2023) Prediction of Diabetes at Early Stage Using Machine Learning Algorithms. *BCP Business & Management*, **38**, 1838-1843. https://doi.org/10.54691/bcpbm.v38i.3978

[6] Li, G., Kujawski, W. and Rynkowska, E. (2020) Advancements in Proton Exchange Membranes for High-Performance High-Temperature Proton Exchange Membrane

Fuel Cells (HT-PEMFC). *Reviews in Chemical Engineering*, **38**, 327-346. https://doi.org/10.1515/revce-2019-0079

[7] Ma, Y., Chen, Y., Sun, M. and Zhang, Y. (2022) Physicochemical Properties of High-entropy Oxides. *The Chemical Record*, **23**, e202200195. https://doi.org/10.1002/tcr.202200195

[8] Gu, X., Guo, X., Li, W., Jiang, Y., Liu, Q. and Tang, X. (2024) High-Entropy Materials for Application: Electricity, Magnetism, and Optics. *ACS Applied Materials & Interfaces*, **16**, 53372-53392. https://doi.org/10.1021/acsami.4c11898

[9] Kotsonis, G.N., Almishal, S.S.I., Marques dos Santos Vieira, F., Crespi, V.H., Dabo, I., Rost, C.M., *et al.* (2023) High-Entropy Oxides: Harnessing Crystalline Disorder for Emergent Functionality. *Journal of the American Ceramic Society*, **106**, 5587-5611. https://doi.org/10.1111/jace.19252

[10] Jia, C., Zhang, L., Peng, X., Luo, J., Zhao, Y., Liu, J., *et al.* (2019) Prediction of Entropy and Gibbs Free Energy for Nitrogen. *Chemical Engineering Science*, **202**, 70-74. https://doi.org/10.1016/j.ces.2019.03.033

[11] Wang, R., Tang, Y., Li, S., Ai, Y., Li, Y., Xiao, B., *et al.* (2020) Effect of Lattice Distortion on the Diffusion Behavior of High-Entropy Alloys. *Journal of Alloys and Compounds*, **825**, Article ID: 154099. https://doi.org/10.1016/j.jallcom.2020.154099

[12] Chang, C., Lu, Y. and Tuan, H. (2023) High-Entropy NaCl-Type Metal Chalcogenides as K-Ion Storage Materials: Role of the Cocktail Effect. *Energy Storage Materials*, **59**, Article ID: 102770. https://doi.org/10.1016/j.ensm.2023.102770

[13] Zhang, H., Tian, J., Cui, X., Li, J. and Zhu, Z. (2023) Highly Mesoporous Carbon Nanofiber Electrodes with Ultrahigh Specific Surface Area for Efficient Capacitive Deionization. *Carbon*, **201**, 920-929. https://doi.org/10.1016/j.carbon.2022.10.002

[14] Koderman Podboršek, G., Zupančič, Š., Kaufman, R., Surca, A.K., Marsel, A., Pavlišič, A., *et al.* (2022) Microstructure and Electrical Conductivity of Electrospun Titanium Oxynitride Carbon Composite Nanofibers. *Nanomaterials*, **12**, Article 2177. https://doi.org/10.3390/nano12132177

[15] Wang, M., Miao, X., Hou, C., Xu, K., Ke, Z., Dai, F., *et al.* (2024) Devisable Pore Structures and Tunable Thermal Management Properties of Aerogels Composed of Carbon Nanotubes and Cellulose Nanofibers with Various Aspect Ratios. *Carbohydrate Polymers*, **323**, Article ID: 121437. https://doi.org/10.1016/j.carbpol.2023.121437

[16] Liang, K., Guo, W., Li, L., Cai, H., Zhang, H., Li, J., *et al.* (2024) Defect-induced Synthesis of Nanoscale Hierarchically Porous Metal-Organic Frameworks with Tunable Porosity for Enhanced Volatile Organic Compound Adsorption. *Nano Materials Science*, **6**, 467-474. https://doi.org/10.1016/j.nanoms.2023.10.001

[17] Gupta, S., Zhao, S., Ogoke, O., Lin, Y., Xu, H. and Wu, G. (2017) Engineering Favorable Morphology and Structure of F-N-C Oxygen-Reduction Catalysts through Tuning of Nitrogen/Carbon Precursors. *ChemSusChem*, **10**, 774-785. https://doi.org/10.1002/cssc.201601397

[18] Liu, L., Hu, S. and Gao, K. (2020) Cellulose Nanofiber Based Flexible N-Doped Carbon Mesh for Energy Storage Electrode with Super Folding Endurance. *Materials Today Energy*, **17**, Article ID: 100441. https://doi.org/10.1016/j.mtener.2020.100441

[19] Zhang, J., Liu, Y., Elledge, H., Chen, H., Mannan, M.S. and Mashuga, C.V. (2017) Carbon Nanofiber Explosion Violence and Thermal Stability. *Journal of Thermal Analysis and Calorimetry*, **129**, 221-231. https://doi.org/10.1007/s10973-017-6120-z

[20] Zhu, H., Zhu, Z., Hao, J., Sun, S., Lu, S., Wang, C., *et al.* (2022) High-Entropy Alloy Stabilized Active IR for Highly Efficient Acidic Oxygen Evolution. *Chemical Engineer-*

ing Journal, **431**, Article ID: 133251.
https://doi.org/10.1016/j.cej.2021.133251

[21] Zhan, C., Xu, Y., Bu, L., Zhu, H., Feng, Y., Yang, T., *et al.* (2021) Subnanometer High-Entropy Alloy Nanowires Enable Remarkable Hydrogen Oxidation Catalysis. *Nature Communications*, **12**, Article No. 6261. https://doi.org/10.1038/s41467-021-26425-2

[22] Song, J., Kim, C., Kim, M., Cho, K.M., Gereige, I., Jung, W., *et al.* (2021) Generation of High-Density Nanoparticles in the Carbothermal Shock Method. *Science Advances*, **7**, eabk2984. https://doi.org/10.1126/sciadv.abk2984

[23] Yao, Y., Huang, Z., Xie, P., Lacey, S.D., Jacob, R.J., Xie, H., *et al.* (2018) Carbothermal Shock Synthesis of High-Entropy-Alloy Nanoparticles. *Science*, **359**, 1489-1494. https://doi.org/10.1126/science.aan5412

[24] Shi, Y., Wang, Y., Li, S., Li, R., Cui, Y. and Wang, Y. (2022) Recrystallization Texture Analysis of $FeCoNiCrMnAl_{0.5}$ High-Entropy Alloy Investigated by High-Energy X-Ray Diffraction. *Metals*, **12**, Article 1674. https://doi.org/10.3390/met12101674

[25] Wei, W., Ge, H., Huang, L., Kuang, M., Al-Enizi, A.M., Zhang, L., *et al.* (2017) Hierarchically Tubular Nitrogen-Doped Carbon Structures for the Oxygen Reduction Reaction. *Journal of Materials Chemistry A*, **5**, 13634-13638. https://doi.org/10.1039/c7ta02658g

[26] Chang, C., Hsiao, Y., Chen, Y., Tsai, C., Lee, Y., Ko, P., *et al.* (2022) Lattice Distortion or Cocktail Effect Dominates the Performance of Tantalum-Based High-Entropy Nitride Coatings. *Applied Surface Science*, **577**, Article ID: 151894. https://doi.org/10.1016/j.apsusc.2021.151894

[27] Choma, J., Jagiello, J. and Jaroniec, M. (2021) Assessing the Contribution of Micropores and Mesopores from Nitrogen Adsorption on Nanoporous Carbons: Application to Pore Size Analysis. *Carbon*, **183**, 150-157. https://doi.org/10.1016/j.carbon.2021.07.020

[28] Kang, J., Fu, X., Elsworth, D. and Liang, S. (2020) Impact of Nitrogen Injection on Pore Structure and Adsorption Capacity of High Volatility Bituminous Coal. *Energy & Fuels*, **34**, 8216-8226. https://doi.org/10.1021/acs.energyfuels.0c01223

[29] Zhang, G., Cheng, X., Yang, D., Yu, G., Ma, H., Wang, J., *et al.* (2019) Loofa Sponage Derived Multi-Tubular CuO/CeO_2-ZrO_2 with Hierarchical Porous Structure for Effective Soot Catalytic Oxidation. *Fuel*, **258**, Article ID: 116202. https://doi.org/10.1016/j.fuel.2019.116202

[30] Byun, M., Kim, D., Sung, K., Jung, J., Song, Y., Park, S., *et al.* (2019) Characterization of Copper-Graphite Composites Fabricated via Electrochemical Deposition and Spark Plasma Sintering. *Applied Sciences*, **9**, Article 2853. https://doi.org/10.3390/app9142853

[31] Jin, M., Cheng, L., Zheng, W., Ding, Y., Zhu, Y., Jia, L., *et al.* (2021) Raman Tensor of Graphite: Symmetry of G, D and D'Phonons. *Science China Materials*, **65**, 268-272. https://doi.org/10.1007/s40843-021-1741-0

[32] Fernandez, V., Fairley, N. and Baltrusaitis, J. (2021) Unraveling Spectral Shapes of Adventitious Carbon on Gold Using a Time-Resolved High-Resolution X-Ray Photoelectron Spectroscopy and Principal Component Analysis. *Applied Surface Science*, **538**, Article ID: 148031. https://doi.org/10.1016/j.apsusc.2020.148031

[33] Carvalho, A., Costa, M.C.F., Marangoni, V.S., Ng, P.R., Nguyen, T.L.H. and Castro Neto, A.H. (2021) The Degree of Oxidation of Graphene Oxide. *Nanomaterials*, **11**, Article 560. https://doi.org/10.3390/nano11030560

[34] Kelemen, S.R., Afeworki, M., Gorbaty, M.L., Kwiatek, P.J., Solum, M.S., Hu, J.Z., *et al.* (2002) XPS and ^{15}N NMR Study of Nitrogen Forms in Carbonaceous Solids. *En-*

ergy & Fuels, **16**, 1507-1515. https://doi.org/10.1021/ef0200828

[35] Wu, S., Wang, X., Zhu, Y., He, P., Yu, X., Qin, F., *et al.* (2023) Different Types of Nitrogen-Doped CQDs Loaded by Cop Used as OER Electrocatalysts. *Inorganic Chemistry Communications*, **153**, Article ID: 110872. https://doi.org/10.1016/j.inoche.2023.110872

[36] Qi, C., Zhang, L., Xu, G., Sun, Z., Zhao, A. and Jia, D. (2018) Co@Co_3O_4 Nanoparticle Embedded Nitrogen-Doped Carbon Architectures as Efficient Bicatalysts for Oxygen Reduction and Evolution Reactions. *Applied Surface Science*, **427**, 319-327. https://doi.org/10.1016/j.apsusc.2017.08.209

[37] Hartmann, S.J., Iurchenkova, A.A., Kallio, T. and Fedorovskaya, E.O. (2020) Electrochemical Properties of Nitrogen and Oxygen Doped Reduced Graphene Oxide. *Energies*, **13**, Article 312. https://doi.org/10.3390/en13020312

[38] Dahamni, M.A., Ghamnia, M., Naceri, S.E., Fauquet, C., Tonneau, D., Pireaux, J., *et al.* (2021) Spray Pyrolysis Synthesis of Pure and Mg-Doped Manganese Oxide Thin Films. *Coatings*, **11**, Article 598. https://doi.org/10.3390/coatings11050598

[39] Lin, T., Seshadri, G. and Kelber, J.A. (1997) A Consistent Method for Quantitative XPS Peak Analysis of Thin Oxide Films on Clean Polycrystalline Iron Surfaces. *Applied Surface Science*, **119**, 83-92. https://doi.org/10.1016/s0169-4332(97)00167-0

[40] Xu, X., Chen, Y., Zhou, W., Zhong, Y., Guan, D. and Shao, Z. (2018) Electrocatalysis: Earth-abundant Silicon for Facilitating Water Oxidation over Iron-Based Perovskite Electrocatalyst (Adv. Mater. Interfaces 11/2018). *Advanced Materials Interfaces*, **5**, Article ID: 1870051. https://doi.org/10.1002/admi.201870051

[41] Laïk, B., Richet, M., Emery, N., Bach, S., Perrière, L., Cotrebil, Y., *et al.* (2024) XPS Investigation of Co-Ni Oxidized Compounds Surface Using Peak-On-Satellite Ratio. Application to $Co_{20}Ni_{80}$ Passive Layer Structure and Composition. *ACS Omega*, **9**, 40707-40722. https://doi.org/10.1021/acsomega.4c05082

[42] Xu, M., Lu, J., Sun, Z., Yang, M., Sheng, B., Chen, M., *et al.* (2024) Lanthanum Doping and Surface Li_3Bo_3 Passivating Layer Enabling 4.8 v Nickel-Rich Layered Oxide Cathodes toward High Energy Lithium-Ion Batteries. *Journal of Colloid and Interface Science*, **673**, 386-394. https://doi.org/10.1016/j.jcis.2024.05.236

[43] Glorieux, B., Berjoan, R., Matecki, M., Kammouni, A. and Perarnau, D. (2007) XPS Analyses of Lanthanides Phosphates. *Applied Surface Science*, **253**, 3349-3359. https://doi.org/10.1016/j.apsusc.2006.07.027

[44] Karuppaiah, B., Jeyaraman, A., Chen, S., Chavan, P.R., Karthik, R., Hasan, M., *et al.* (2023) Effect of Bismuth Doping on Zircon-Type Gadolinium Vanadate: Effective Electrocatalyst for Determination of Hazardous Herbicide Mesotrione. *Chemosphere*, **313**, Article ID: 137543. https://doi.org/10.1016/j.chemosphere.2022.137543

[45] Song, X., Schrade, M., Masó, N. and Finstad, T.G. (2017) Zn Vacancy Formation, Zn Evaporation and Decomposition of ZnSb at Elevated Temperatures: Influence on the Microstructure and the Electrical Properties. *Journal of Alloys and Compounds*, **710**, 762-770. https://doi.org/10.1016/j.jallcom.2017.03.339